14

Measurement and modeling of rain intensity and attenuation for the design and evaluation of microwave and millimeter-wave communication systems

Gamantyo Hendrantoro
Institut Teknologi Sepuluh Nopember
Indonesia

Akira Matsushima
Kumamoto University
Japan

1. Introduction

Rain-induced attenuation creates one of the most damaging effects of the atmosphere on the quality of radio communication systems, especially those operating above 10 GHz. Accordingly, methods have been devised to overcome this destructive impact. Adaptive fade mitigation schemes have been proposed to mitigate the rain fade impact in terrestrial communications above 10 GHz (e.g., Sweeney & Bostian, 1999). These schemes mainly deal with the temporal variation of rain attenuation. When such methods as site diversity and multi-hop relaying are to be used, or when the impact of adjacent interfering links is concerned, the spatial variation of rain must also be considered (Hendrantoro et al, 2002; Maruyama et al, 2008; Sakarellos et al, 2009; Panagopoulos et al, 2006). There is also a possibility of employing a joint space-time mitigation technique (Hendrantoro & Indrabayu, 2005). In designing a fade mitigation scheme that is expected to work well within a specified set of criteria, an evaluation technique must be available that is appropriate to test the system performance against rainy channels. Consequently, a model that can emulate the behavior of rain in space and time is desired.

This chapter presents results that have thus far been acquired from an integrated research campaign jointly carried out by researchers at Institut Teknologi Sepuluh Nopember, Indonesia and Kumamoto University, Japan. The research is aimed at devising transmission strategies suitable for broadband wireless access in microwave and millimeter-wave bands, especially in tropical regions. With regards to modeling rain rate and attenuation, the project has gone through several phases, which include endeavors to measure the space-time variations of rain intensity and attenuation (Hendrantoro et al, 2006; Mauludiyanto et al, 2007; Hendrantoro et al, 2007b), to appropriately model them (e.g., Yadnya et al, 2008a;

Yadnya et al, 2008b), and finally to apply the resulting model in evaluation of transmission system designs (e.g., Kuswidiastuti et al, 2008). Tropical characteristics of the measured rain events in Indonesia have been the focus of this project, primarily due to the difficulty in implementing rain-resistant systems in microwave and millimeter-wave bands in tropical regions (Salehudin et al, 1999) and secondarily because of the lack of rain attenuation data and models for these regions. The design of millimeter-wave broadband wireless access with short links, as typified by LMDS (local multipoint distribution services), is also a central point in this project, which later governs the choice of space-time measurement method. As such, endeavors reported in this chapter offer multiple contributions:

a. Measurements and analyses of raindrop size distribution, raindrop fall velocity distribution, rain rate and attenuation in maritime tropical regions represented by the areas of Surabaya.
b. Method to estimate specific attenuation of rain from raindrop size distribution models.
c. Stochastic model of rain attenuation that can be adopted to generate rain attenuation samples for use in evaluation of fade mitigation techniques.

We start in the next section with the measurement system, raindrop size distribution modeling, estimation of specific attenuation, and the synthetic storm technique. Afterward, we discuss modeling of rain intensity and attenuation, touching upon space-time distribution and the time series models. Finally, examples of evaluation of communication systems are given, followed by some concluding remarks.

2. Measurement of rain intensity and attenuation

2.1 Spatio-temporal measurement of rain intensity

The design of our space-time rain field measurement system is based on several criteria. Firstly, the spatial and temporal scope and resolution of the rain field variation must be taken into account. Another constraint is the available budget and technology. When budget is not a concern, space-time measurement using rain radar can be done, as exemplified by Tan and Goddard (1998) and Hendrantoro and Zawadzki (2003). Radar has its strength in large observation area and feasibility of simulating radio links on radar image. However, due to its weaknesses that include high cost and low time resolution, and due to the relatively small measurement area desired to emulate an LMDS cell, it is decided to employ a network of synchronized rain gauges operated within the campus area of Institut Teknologi Sepuluh Nopember (ITS) in Surabaya, as shown in Fig. 1. The longest distance between rain gauges is about 1.55 km, from site A at the Polytechnic building to site D at the Medical Center. The shortest, about 400 m, is between site B at the Department of Electrical Engineering building and site C at the Library building. The rain gauges, each of tipping-bucket type, are synchronized manually. At site B, an optical-type Parsivel disdrometer is also operated to record the drop size distribution (DSD), as well as a 54-meter radio link at 28 GHz adopted to measure directly rain attenuation.

2.2 Raindrop size distribution measurement and modelling

DSD (raindrop size distribution) is a fundamental parameter that directly affects rainfall rate and rain-induced attenuation. The widely used negative exponential model of DSD

proposed by Marshall and Palmer (1948) derived from measurement in North America might yield inaccurate statistical estimates of rain rate and attenuation when adopted for tropical regions (Yeo et al, 1993). A number of tropical DSD measurements have since been reported and models proposed accordingly. Nevertheless, considering the variety of geographical situations of regions within the tropical belt, each with its own regional sub-climate, more elaborate studies on tropical DSD are deemed urgent.

In this study, we use Parsivel, an optical-type disdrometer that works on a principle of detecting drops falling through the horizontal area of a laser beam. As a result, the instrument is capable of measuring not only the diameter of each falling drop but also its fall velocity. The system consists of the optical detector connected to a computer that records the raw data. Each record comprises the number of detected drops within a certain diameter interval and fall velocity interval. The average DSD ($m^{-3}mm^{-1}$) can be obtained as:

$$\overline{N}(D) = \frac{C(D)}{AT\Delta D}\left(\frac{1}{C(D)}\sum_{k=1}^{C(D)}\frac{1}{v_k(D)}\right) \tag{1}$$

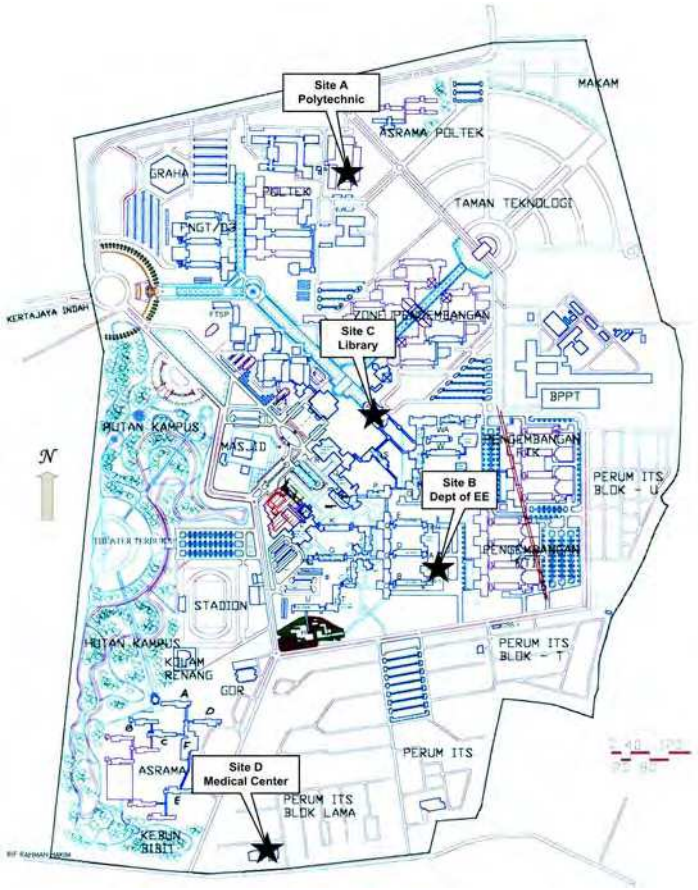

Fig. 1. Map of the measurement area in the campus of ITS in Surabaya.

where $C(D)$ denotes the number of drops detected in the diameter interval $[D-\Delta D/2, D+\Delta D/2)$ given in millimeters, A (m^2) the area of the laser beam, T (seconds) the integration time, $v_k(D)$ the measured velocity in m/s of the k^{th} drop in the diameter interval $[D-\Delta D/2, D+\Delta D/2)$, as opposed to a deterministic diameter-dependent velocity model such as the Gunn-Kinzer (Brussaard & Watson, 1995). From (1) it is apparent that the average DSD is a linear function of the average of the inverse of drop fall velocity, rather than the average velocity itself. This can cause discrepancy of attenuation or radar reflectivity estimates from their actual values. In fact, measurements made using a similar instrument in the US reveal discrepancy of the average fall velocity from the theoretical deterministic value (Tokay et al, 2003). The variations of raindrop fall velocity will be discussed later in this section. In our study, DSD measurements are categorized into bins representing disjoint intervals of rainfall rate, 0-0.5, 0.5-1, 1-2, …, 256-512 mm/h. An average DSD and an average rain rate are subsequently computed for each bin. Table 1 summarizes the parameter values for each interval. Although the Parsivel is able to detect objects of larger diameters, only those within the diameter range up to 6 mm, relevant to the maximum diameter of stable raindrops (Brussaard & Watson, 1995), are considered. The sampling volume in the table is calculated by assuming the Gunn-Kinzer fall velocity and using the fact that the laser beam area is 3 cm × 18 cm. Table 2 recapitulates the DSD measurements made in Surabaya for the various bins of rain rate. Fig. 2 presents the average DSD curves for all rain rate bins.

Singapore and Surabaya are located in the same region of Southeast Asia and share the same tropical maritime climate. Three models fitted to Singapore DSD reported in the literature are used in this study, two of which are lognormal and gamma fitted to measurements made by Ong et al using a Joss-Waldvogel disdrometer (Timothy et al, 2002). The other is a negative exponential model obtained using the indirect method in which the DSD shape is assumed a priori and it is only the shape parameters that are estimated by fitting the DSD model to measurements of rainfall rate and attenuation (Yeo et al, 1993, Li et al, 1994). The Marshal-Palmer model is also included in the comparison. The DSD evaluation is made for three different values of average rain rate, 11.068, 44.15, and 174 mm/h, representing low, medium, and high intensity, respectively.

As shown in Fig. 3 in general the Surabaya curve stays constantly below the Marshall-Palmer. Comparison with the Singapore models show that, except for the gamma model, the higher the rain rate, the larger the difference between the Singapore models and the Surabaya results, with the Surabaya DSD falling below the Singapore results for almost all drop diameters. For lower rain rates, the difference is not large and Surabaya DSD shows larger concentration of drops with larger diameters yet fewer smaller drops. A previous study in North America reported by Hendrantoro and Zawadzki (2003) has found that contribution to attenuation at 30 GHz is dominated by drops of diameters in the 1-3 mm range. This observation suggests that for the same rain rate the induced attenuation at 30 GHz in Surabaya might be lower on average than that in Singapore. It should be stressed herein that all of these disagreements in the detailed shapes of Surabaya DSD from that of either Singapore or Marshall-Palmer might originate from differences in various aspects of the measurement, such as the local climate, the measuring instrument, the number of samples, and the year of measurement. A more in-depth study is required to identify the real causes of the disagreements.

Central Diameter (D, mm)	Interval Width (ΔD, mm)	Sampling Volume (m^3)	
		T = 10 s	T = 60 s
0.062	0.125	0.0058	0.0349
0.187	0.125	0.0357	0.2143
0.312	0.125	0.0661	0.3966
0.437	0.125	0.0965	0.5788
0.562	0.125	0.1252	0.7510
0.687	0.125	0.1522	0.9130
0.812	0.125	0.1792	1.0750
0.937	0.125	0.2062	1.2370
1.062	0.125	0.2292	1.3753
1.187	0.125	0.2477	1.4862
1.375	0.250	0.2742	1.6450
1.625	0.250	0.3068	1.8410
1.875	0.250	0.3366	2.0198
2.125	0.250	0.3636	2.1814
2.375	0.250	0.3876	2.3258
2.750	0.500	0.4183	2.5101
3.250	0.500	0.4493	2.6956
3.750	0.500	0.4641	2.7845
4.250	0.500	0.4641	2.7845
4.750	0.500	0.4641	2.7845
5.500	1.000	0.4641	2.7845

Table 1. Interval Parameter Values of the Optical Disdrometer.

Rain rate interval (mm/hr)	Center value (mm/hr)	Average value (mm/hr)	Number of samples
0 – 0.5	0.25	0.1162	7116
0.5 – 1	0.75	0.7089	1168
1 – 2	1.5	1.447	829
2 – 4	3	2.799	957
4 – 8	6	5.640	892
8 – 16	12	11.06	420
16 – 32	24	22.12	471
32 – 64	48	44.15	382
64 – 128	96	90.19	212
128 – 256	192	174.9	169
256 – 512	384	257.2	80

Table 2. Number of Measured Samples in Each Rain Rate Bin.

For model fitting purpose, the average DSD curves for the lowest two intervals of rain rate are excluded due to irregularities in their shapes that hinder achievement of a good fit to each of the adopted models. This treatment does not bear any significant implication to the

design of millimeter-wave communications since rain events of high intensity are of higher importance. The DSD measurements are fitted to a number of theoretical models, namely, the negative exponential, Weibull, and gamma. Among the three, gamma fits worst, and therefore is not discussed further herein. On the other hand, Weibull slightly outdoes the negative exponential and yields the following equation:

$$N(D) = 281.629 \frac{\eta}{\sigma} \left(\frac{D}{\sigma} \right)^{\eta - 1} \exp\left[- \left(\frac{D}{\sigma} \right)^{\eta} \right] \tag{2}$$

with $\eta = 1.212 R^{0.056}$ and $\sigma = 0.728 R^{0.177}$. Whereas the negative exponential fit gives:

$$N(D) = 1054 \exp(-2.415 R^{-0.14} D) \tag{3}$$

where $N(D)$ is the DSD given in $m^{-3}mm^{-1}$ with the drop diameter D expressed in mm and rain rate R in mm/hr.

An examination is also made on the variation of raindrop fall velocity. The Gunn-Kinzer velocity model commonly adopted in the computation of specific attenuation from DSD was obtained from an experiment in an ideal environment. It is therefore of interest to see the actual variation of rainfall velocity and its impact on the rain attenuation induced. Fig. 4 (a) depicts the average fall velocity as detected by the disdrometer for each diameter range compared with that of Gunn-Kinzer. There can be observed a discrepancy for large drops from the Gunn-Kinzer estimate. The probability density function of fall velocity for diameter range of central value 6.5 mm, shown in Fig. 4 (b), indicates as if a large number of drops fall with near-zero velocity. To a lesser extent the same trend can also be observed for other diameter ranges. A correction attempt is made accordingly by omitting drops with velocities that are considered too low for their size. This is done to velocity ranges $v(D) \le 4$ m/s for 4.25 mm $\le D \le$ 6.5 mm, $v(D) \le 2$ m/s for 3.25 mm $\le D \le$ 3.75 mm, and $v(D) \le 1$ m/s for 1.062 mm $\le D \le$ 2.75 mm, and is referred to as correction #1. A second attempt (correction #2) is made by linearizing the density function for velocity ranges stated above starting from zero at zero velocity. Despite the discrepancy of the velocity measurement from that of the Gunn-Kinzer and various corrections thereof (Fig. 4 (c)), it is found that the resulting discrepancy in specific attenuation from that obtained using the Gunn-Kinzer velocity is not significant, as given in Table 3. It is therefore considered safe to use Gunn-Kinzer velocity in subsequent analysis of rain attenuation.

Y_h	Average error magnitude (dB/km)
Measurement	0.0725
Correction #1	0.0250
Correction #2	0.0210

Table 3. Average error magnitude of attenuation for horizontally-polarized waves (Y_h).

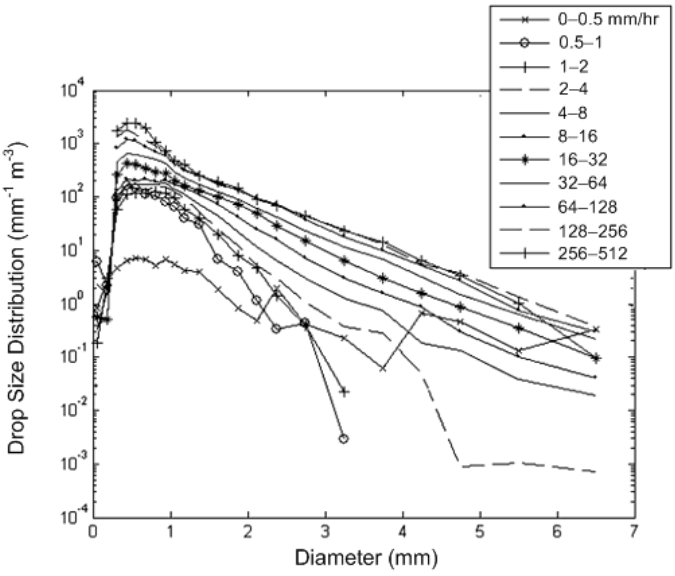

Fig. 2. Curves of average DSD for different intervals of rain rate obtained from measurements made in Surabaya.

2.3 Rain intensity-to-specific attenuation conversion

a. Formulation as scattering problem

Although realistic raindrops are modelled as a deformed body of revolution (Pruppacher et al., 1971), we limit the analysis here to the most fundamental spherical shape. Nevertheless, the final conversion formula is still valid once we could obtain the modal coefficients of far scattered field emerged from arbitrarily shaped body.

As shown in Fig. 5, a set of dielectric spheres having a common relative permittivity ε_r is arbitrarily distributed in the air. The number of spheres is Q, and each has an arbitrary radius a_q (q = 1, 2, ..., Q). A position vector is given by $\boldsymbol{r} = \hat{x}x + \hat{y}y + \hat{z}z = r\left(\hat{x}\sin\theta\cos\phi + \hat{y}\sin\theta\sin\phi + \hat{z}\cos\theta\right)$, where $\hat{x}$, $\hat{y}$, and $\hat{z}$ are the unit vectors concerning respective coordinate variables. The center of p-th sphere 0_p is denoted by $\boldsymbol{r} = \boldsymbol{r}_{p0} = \hat{x}x_{p0} + \hat{y}y_{p0} + \hat{z}z_{p0}$. A position is often measured in terms of the local spherical coordinate system $\left(r_p, \theta_p, \phi_p\right)$ with its center located at 0_p as

$$\boldsymbol{r}_p = \boldsymbol{r} - \boldsymbol{r}_{p0} = r_p\left(\hat{x}\sin\theta_p\cos\phi_p + \hat{y}\sin\theta_p\sin\phi_p + \hat{z}\cos\theta_p\right) \tag{4}$$

Let us decompose the total electromagnetic fields as

$$(\boldsymbol{E},\boldsymbol{H})=\begin{cases}\left(\left(\boldsymbol{E}^{i},\boldsymbol{H}^{i}\right)+\sum_{q=1}^{Q}\left(\boldsymbol{E}^{s(q)},\boldsymbol{H}^{s(q)}\right)\right) & \text{(in the air)}\\ \left(\boldsymbol{E}^{d(p)},\boldsymbol{H}^{d(p)}\right) & \text{(in } p\text{ - th sphere: } p=1,2,...,Q)\end{cases} \tag{5}$$

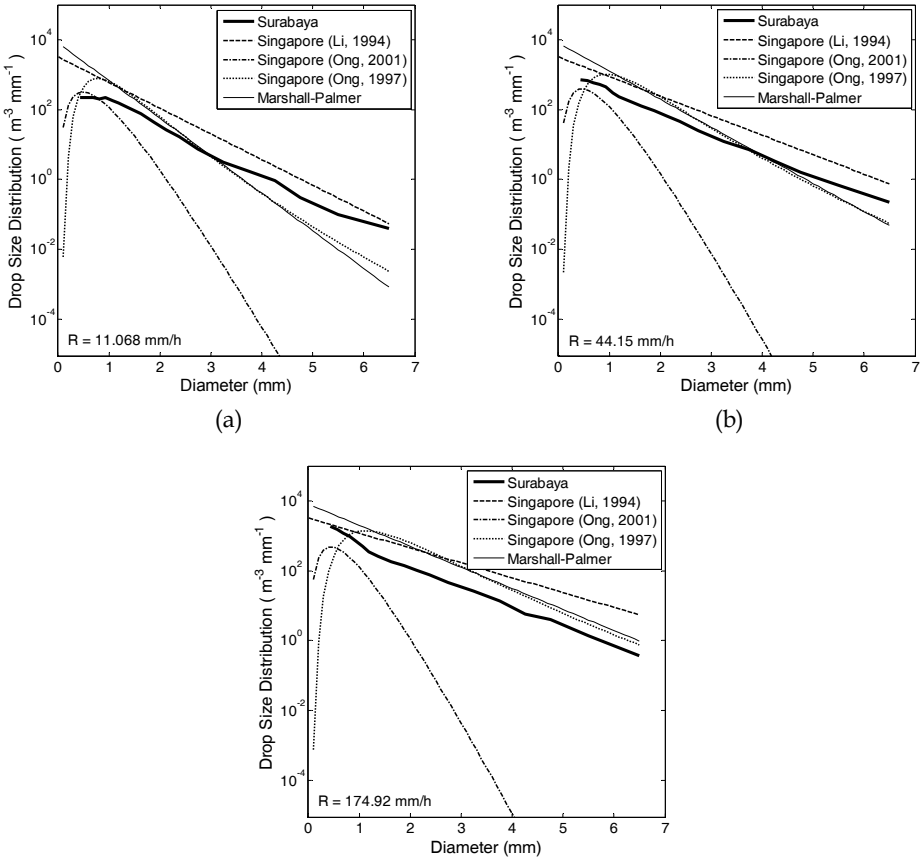

Fig. 3. Comparison of drop size distributions measured in Surabaya and models derived from measurements in Singapore for various rain rates: (a) 11.068 mm/h, (b) 44.15 mm/h, and (c) 174.92 mm/h, which for the Surabaya measurement are average values of intervals 8-16, 32-64, and 128-256 mm/h, respectively.

where the superscripts *i*, *s*(*q*), and *d*(*p*) concern the incident field, the scattered field due to the existence of the sphere #*q*, and the field inside the sphere #*p*, respectively. With no loss of generality, we can assume that the incident field is *x*-polarized and propagates in the +*z*

direction. Omitting the time factor $e^{j\omega t}$, we have the expression $E_x^i(\boldsymbol{r}) = \zeta_0 H_y^i(\boldsymbol{r}) = e^{-jk_0 z}$, where $k_0 = \omega\sqrt{\varepsilon_0\mu_0}$ and $\zeta_0 = \sqrt{\mu_0/\varepsilon_0}$.

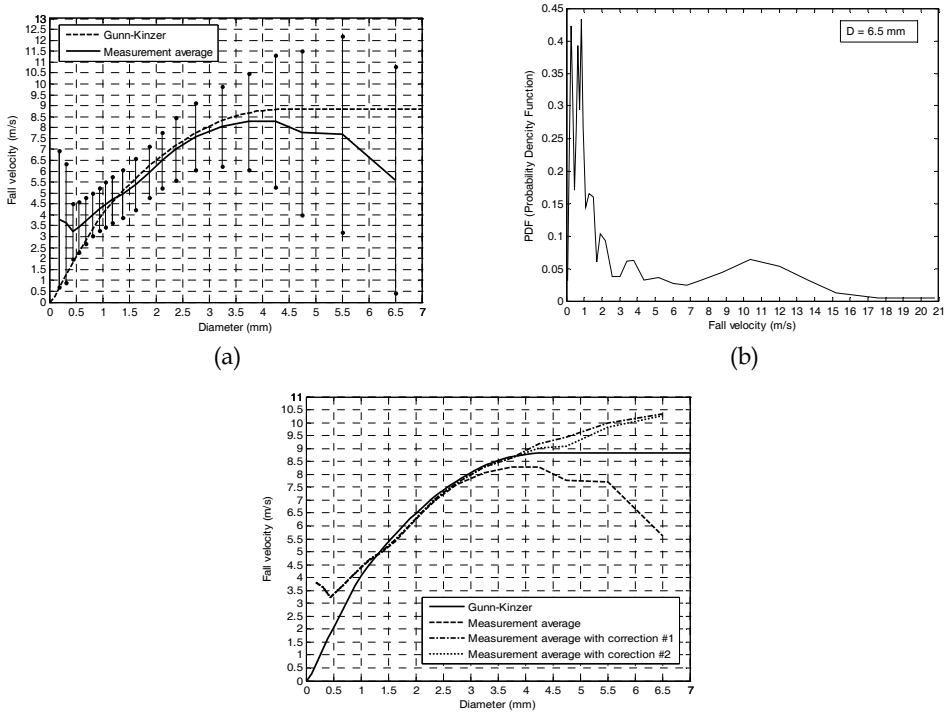

Fig. 4. Drop fall velocity variations shown by (a) the mean ± variance of fall velocity for every diameter bin, (b) the density function of fall velocity for drop of 6.5 mm diameter and (c) fall velocity curves with corrections.

b. Expression of electromagnetic fields

Let us express the electromagnetic fields in the right hand side of (5) as

$$\begin{pmatrix} \boldsymbol{E}^i(\boldsymbol{r}) \\ -j\zeta_0 \boldsymbol{H}^i(\boldsymbol{r}) \end{pmatrix} = e^{-jk_0 z_{p0}} \sum_{n=1}^{\infty} \sum_{m=-n}^{n} \begin{pmatrix} V_{mn} & U_{mn} \\ U_{mn} & V_{mn} \end{pmatrix} \begin{pmatrix} \boldsymbol{M}_{mn}^{(1)}(k_0 r_p, \theta_p, \phi_p) \\ \boldsymbol{N}_{mn}^{(1)}(k_0 r_p, \theta_p, \phi_p) \end{pmatrix} \tag{6}$$

$$\begin{pmatrix} \boldsymbol{E}^{s(q)}(\boldsymbol{r}) \\ -j\zeta_0 \boldsymbol{H}^{s(q)}(\boldsymbol{r}) \end{pmatrix} = \sum_{n=1}^{\infty} \sum_{m=-n}^{n} \begin{pmatrix} B_{qmn} & A_{qmn} \\ A_{qmn} & B_{qmn} \end{pmatrix} \begin{pmatrix} \boldsymbol{M}_{mn}^{(4)}(k_0 r_q, \theta_q, \phi_q) \\ \boldsymbol{N}_{mn}^{(4)}(k_0 r_q, \theta_q, \phi_q) \end{pmatrix} \tag{7}$$

$$\begin{pmatrix} \boldsymbol{E}^{d(p)}(\boldsymbol{r}) \\ -j\zeta \boldsymbol{H}^{d(p)}(\boldsymbol{r}) \end{pmatrix} = \sum_{n=1}^{\infty} \sum_{m=-n}^{n} \begin{pmatrix} D_{pmn} & C_{pmn} \\ C_{pmn} & D_{pmn} \end{pmatrix} \begin{pmatrix} \boldsymbol{M}_{mn}^{(1)}(kr_p, \theta_p, \phi_p) \\ \boldsymbol{N}_{mn}^{(1)}(kr_p, \theta_p, \phi_p) \end{pmatrix} \tag{8}$$

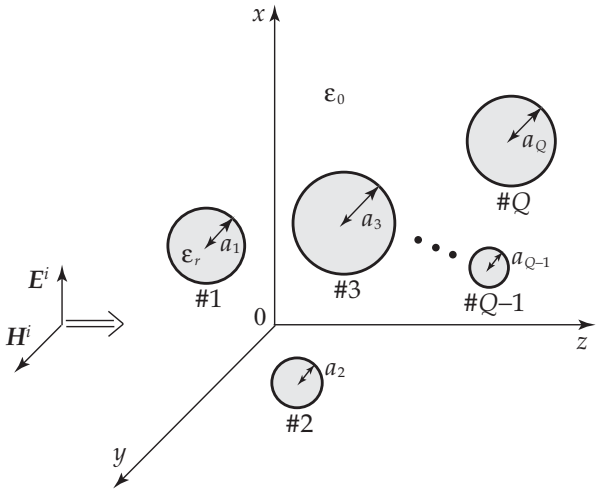

Fig. 5. Dielectric spheres and incident field.

where $k=\omega\sqrt{\varepsilon_0\varepsilon_r\mu_0}$ and $\zeta=\sqrt{\mu_0/(\varepsilon_0\varepsilon_r)}$. The vector spherical wave functions are defined as (Stratton, 1941)

$$\boldsymbol{M}_{mn}^{(l)}(\rho,\theta,\phi)=\frac{\hat{Z}_n^{(l)}(\rho)}{\rho}\boldsymbol{m}_{mn}(\theta,\phi) \tag{9}$$

$$\boldsymbol{N}_{mn}^{(l)}(\rho,\theta,\phi)=\frac{jn(n+1)}{\rho^2}\hat{Z}_n^{(l)}(\rho)\sin\theta\,\pi_n^{|m|}(\theta)e^{jm\phi}\,\hat{r}+\frac{\hat{Z}_n^{(l)\prime}(\rho)}{\rho}\boldsymbol{n}_{mn}(\theta,\phi) \tag{10}$$

where

$$\boldsymbol{m}_{mn}(\theta,\phi)=\left[-m\pi_n^{|m|}(\theta)\hat{\theta}-j\tau_n^{|m|}(\theta)\hat{\phi}\right]e^{jm\phi},\qquad \boldsymbol{n}_{mn}=\hat{r}\times\boldsymbol{m}_{mn} \tag{11}$$

with the associated Legendre functions $\pi_n^m(\theta)=P_n^m(\cos\theta)/\sin\theta$, $\tau_n^m(\theta)=dP_n^m(\cos\theta)/d\theta$, and the spherical Bessel functions $\hat{Z}_n^{(l)}(\rho)=\sqrt{\pi\rho/2}\,Z_{n+1/2}^{(l)}(\rho)$. The function $Z_n^{(l)}$ corresponds to the cylindrical functions J_n, Y_n, $H_n^{(1)}$, and $H_n^{(2)}$ for l = 1, 2, 3, and 4, respectively. The prime denotes derivative with respect to the variable. As for the incident wave of (6), the spherical wave expansion of a plane wave gives

$$U_{mn}=-\mathrm{sgn}(m)V_{mn}=-j^{-n}(2n+1)\delta_{|m|1}/[2n(n+1)] \tag{12}$$

with $\delta_{|m|1}$ being Kronecker's delta.

c. Mode matching method

The boundary conditions on the dielectric surface are written as

$$\hat{r}_p \times \left(\boldsymbol{F}^i(\boldsymbol{r}) + \sum_{q=1}^{Q} \boldsymbol{F}^{s(q)}(\boldsymbol{r}) - \boldsymbol{F}^{d(p)}(\boldsymbol{r}) \right) \Bigg|_{r_p = a_p} = 0 \qquad \left(0 \le \theta_p \le \pi, 0 \le \phi_p < 2\pi; p = 1, 2, ..., Q\right) \tag{13}$$

where $\boldsymbol{F}$ stands for $\boldsymbol{E}$ and $\boldsymbol{H}$. We substitute (6)-(8) into (13) and truncate the infinite series at $n = N_q$ for the q-th sphere (q = 1, 2, …, Q). The values N_q depend on the electrical size of spheres. This leads us to linear equations including $4\sum_{q=1}^{Q} N_q\left(N_q + 2\right)$ unknown coefficients A_{qmn}, B_{qmn}, C_{pmn}, and D_{pmn}.

As seen from (6)-(8), the origins of observation points are not unified at this stage. In order to shift the origin of $\boldsymbol{E}^{s(q)}$ and $\boldsymbol{H}^{s(q)}$ from 0_q to 0_p, we apply the addition theorem for vector spherical wave functions (Cruzan, 1962)

$$\begin{pmatrix} \boldsymbol{M}_{mn}^{(4)}\left(k_0 \boldsymbol{r}_q\right) \\ \boldsymbol{N}_{mn}^{(4)}\left(k_0 \boldsymbol{r}_q\right) \end{pmatrix} = \sum_{\nu=1}^{\infty} \sum_{\mu=-\nu}^{\nu} \begin{pmatrix} \alpha_{mn,\mu\nu}^{(4)}\left(k_0 \boldsymbol{r}_{pq}\right) & \beta_{mn,\mu\nu}^{(4)}\left(k_0 \boldsymbol{r}_{pq}\right) \\ \beta_{mn,\mu\nu}^{(4)}\left(k_0 \boldsymbol{r}_{pq}\right) & \alpha_{mn,\mu\nu}^{(4)}\left(k_0 \boldsymbol{r}_{pq}\right) \end{pmatrix} \begin{pmatrix} \boldsymbol{M}_{\mu\nu}^{(1)}\left(k_0 \boldsymbol{r}_p\right) \\ \boldsymbol{N}_{\mu\nu}^{(1)}\left(k_0 \boldsymbol{r}_p\right) \end{pmatrix} \tag{14}$$

where the position $\left(k_0 r_p, \theta_p, \phi_p\right)$ has been simply written as $k_0 \boldsymbol{r}_p$. The translation coefficients $\alpha_{mn,\mu\nu}^{(4)}$ and $\beta_{mn,\mu\nu}^{(4)}$ are the functions of the shift vector $\boldsymbol{r}_{pq} = \boldsymbol{r}_{p0} - \boldsymbol{r}_{q0}$. Making use of the orthogonal properties of the vector spherical wave functions, and eliminating the coefficients $C_{p\mu\nu}$ and $D_{p\mu\nu}$, we arrive at the set of linear equations

$$\left.\begin{aligned} A_{p\mu\nu} - \sum_{q=1(\neq p)}^{Q} \sum_{n=1}^{N_q} \sum_{m=-n}^{n} \left[A_{qmn} \alpha_{mn,\mu\nu}^{(4)}\left(k_0 \boldsymbol{r}_{pq}\right) + B_{qmn} \beta_{mn,\mu\nu}^{(4)}\left(k_0 \boldsymbol{r}_{pq}\right) \right] \overline{A}_{p\nu} = U_{\mu\nu} \overline{A}_{p\nu} e^{-jk_0 z_{p0}} \\ B_{p\mu\nu} - \sum_{q=1(\neq p)}^{Q} \sum_{n=1}^{N_q} \sum_{m=-n}^{n} \left[A_{qmn} \beta_{mn,\mu\nu}^{(4)}\left(k_0 \boldsymbol{r}_{pq}\right) + B_{qmn} \alpha_{mn,\mu\nu}^{(4)}\left(k_0 \boldsymbol{r}_{pq}\right) \right] \overline{B}_{p\nu} = V_{\mu\nu} \overline{B}_{p\nu} e^{-jk_0 z_{p0}} \end{aligned}\right\} \tag{15}$$

$$\left(\nu = 1, 2, ..., N_p; \mu = -\nu, -\nu + 1, ..., \nu; p = 1, 2, ..., Q\right)$$

where

$$\overline{A}_{p\nu} = -\frac{\hat{J}_\nu\left(k_0 a_p\right) \hat{J}_\nu'\left(k a_p\right) - \sqrt{\varepsilon_r}\, \hat{J}_\nu'\left(k_0 a_p\right) \hat{J}_\nu\left(k a_p\right)}{\hat{H}_\nu^{(2)}\left(k_0 a_p\right) \hat{J}_\nu'\left(k a_p\right) - \sqrt{\varepsilon_r}\, \hat{H}_\nu^{(2)\prime}\left(k_0 a_p\right) \hat{J}_\nu\left(k a_p\right)} \tag{16}$$

$$\overline{B}_{p\nu} = -\frac{\hat{J}_\nu'\left(k_0 a_p\right) \hat{J}_\nu\left(k a_p\right) - \sqrt{\varepsilon_r}\, \hat{J}_\nu\left(k_0 a_p\right) \hat{J}_\nu'\left(k a_p\right)}{\hat{H}_\nu^{(2)\prime}\left(k_0 a_p\right) \hat{J}_\nu\left(k a_p\right) - \sqrt{\varepsilon_r}\, \hat{H}_\nu^{(2)}\left(k_0 a_p\right) \hat{J}_\nu'\left(k a_p\right)} \tag{17}$$

Equation (15) includes the same number of relations as that of unknowns, and thereby, is numerically solved. After that, the other coefficients are computed from

$$C_{p\mu\nu} = \overline{C}_{p\nu} A_{p\mu\nu} / \overline{A}_{p\nu}, \qquad \mathrm{D}_{p\mu\nu} = \overline{D}_{p\nu} B_{p\mu\nu} / \overline{B}_{p\nu} \tag{18}$$

where

$$\overline{C}_{p\nu} = \frac{j\sqrt{\varepsilon_r}}{\widehat{H}_\nu^{(2)}\left(k_0 a_p\right)\widehat{J}_\nu{}'\left(ka_p\right) - \sqrt{\varepsilon_r}\,\widehat{H}_\nu^{(2)\prime}\left(k_0 a_p\right)\widehat{J}_\nu\left(ka_p\right)} \tag{19}$$

$$\overline{D}_{p\nu} = -\frac{j\sqrt{\varepsilon_r}}{\widehat{H}_\nu^{(2)\prime}\left(k_0 a_p\right)\widehat{J}_\nu\left(ka_p\right) - \sqrt{\varepsilon_r}\,\widehat{H}_\nu^{(2)}\left(k_0 a_p\right)\widehat{J}_\nu{}'\left(ka_p\right)} \tag{20}$$

Equations (16), (17), (19), and (20) are called Mie's coefficients (Harrington, 1961). It should be noted that the terms including the translation coefficients in (15) represent the effect of multiple scattering among spheres. If raindrops are so sparsely distributed that the multiple effect is very weak, the approximate solutions of (15) are directly derived as

$$A_{qmn} \approx U_{mn}\overline{A}_{qn}e^{-jk_0 z_{q0}}, \quad \mathrm{B}_{qmn} \approx V_{mn}\overline{B}_{qn}e^{-jk_0 z_{q0}} \tag{21}$$

d. Scattering and absorption cross sections

Employing the large argument approximations $\widehat{H}_n^{(2)}\left(k_0 r_q\right) \approx j\widehat{H}_n^{(2)\prime}\left(k_0 r_q\right) \approx j^{n+1}e^{-jk_0 r_q}$ and $r_q = r - \boldsymbol{r}\cdot\boldsymbol{r}_{q0}/r$ in (7), we can write the far scattered field in the form of inhomogeneous spherical waves as

$$\begin{pmatrix} E_\theta^s(\boldsymbol{r}) \\ E_\phi^s(\boldsymbol{r}) \end{pmatrix} \approx \zeta_0 \begin{pmatrix} H_\phi^s(\boldsymbol{r}) \\ -H_\theta^s(\boldsymbol{r}) \end{pmatrix} \approx \frac{e^{-jk_0 r}}{k_0 r}\begin{pmatrix} f_\theta(\theta,\phi) \\ f_\phi(\theta,\phi) \end{pmatrix} \quad (r \to \infty) \tag{22}$$

where the scattering pattern functions are

$$\begin{pmatrix} f_\theta(\theta,\phi) \\ f_\phi(\theta,\phi) \end{pmatrix} = \sum_{q=1}^{Q}\sum_{n=1}^{N_q}\sum_{m=-n}^{n} j^n\left(A_{qmn}\,\widehat{\theta} + jB_{qmn}\,\widehat{\phi}\right)\cdot\begin{pmatrix} \boldsymbol{n}_{mn}(\theta,\phi) \\ \boldsymbol{m}_{mn}(\theta,\phi) \end{pmatrix} e^{-jk_0\boldsymbol{r}\cdot\boldsymbol{r}_{q0}/r} \tag{23}$$

The total scattered power is computed from

$$\begin{aligned} P^s &= \frac{1}{2}\mathrm{Re}\left[\int_0^{2\pi}\int_0^{\pi}\left[\boldsymbol{E}^s(\boldsymbol{r})\times\boldsymbol{H}^{s^*}(\boldsymbol{r})\right]\cdot\hat{r}\Big|_{r\to\infty} r^2\sin\theta\, d\theta\, d\phi\right] \\ &\approx \frac{1}{2\zeta_0 k_0^2}\int_0^{2\pi}\int_0^{\pi}\left[\left|f_\theta(\theta,\phi)\right|^2 + \left|f_\phi(\theta,\phi)\right|^2\right]\sin\theta\, d\theta\, d\phi \end{aligned} \tag{24}$$

where the asterisk denotes complex conjugate. The integrals with respect to θ and ϕ in above are numerically evaluated by the Gauss-Legendre quadrature rule and the trapezoidal formula, respectively. Since the power density of incident field is $W^i = 1/(2\zeta_0)$, the total scattering cross section is given by $\sigma^s = P^s / W^i = 2\zeta_0 P^s$.

On the other hand, the power absorbed inside the spheres is computed from

$$
\begin{aligned}
P^a &= \frac{1}{2}\mathrm{Re}\sum_{q=1}^{Q}\left[\int_0^{2\pi}\int_0^{\pi}\left[\boldsymbol{E}^{d(q)}(\boldsymbol{r})\times\boldsymbol{H}^{d(q)*}(\boldsymbol{r})\right]\cdot(-\hat{r})\Big|_{r\to a_q} a_q^2\sin\theta\, d\theta\, d\phi\right] \\
&\approx \frac{\pi}{k_0^2\zeta_0}\mathrm{Re}\frac{1}{j\sqrt{\varepsilon_r}}\sum_{n=1}^{N_q}\sum_{m=-n}^{n}\frac{2n(n+1)(n+m)!}{(2n+1)(n-m)!} \\
&\quad\times\sum_{q=1}^{Q}\left[\left|C_{qmn}\right|^2\hat{J}_n'(ka_q)\hat{J}_n^*(ka_q)-\left|D_{qmn}\right|^2\hat{J}_n(ka_q)\hat{J}_n^{*\prime}(ka_q)\right]
\end{aligned}
\tag{25}
$$

The absorption cross section is given by $\sigma^a = P^a / W^i = 2\zeta_0 P^a$.

The optical theorem or the extinction theorem states that the diffracted field in the forward direction, which is related to $f_\theta(0,0)$, should be attenuated due to the scattering and absorption. This is based on the law of energy conservation. The amount of this attenuation is called the extinction cross section and expressed as

$$
\begin{aligned}
\sigma^e &= \sigma^s + \sigma^a = -\frac{4\pi}{k_0^2}\mathrm{Im}\left[f_\theta(0,0)\right] \\
&= \frac{2\pi}{k_0^2}\sum_{n=1}^{N_q} n(n+1)\,\mathrm{Im}\left\{j^{n+1}\sum_{q=1}^{Q}\left[A_{q1n}+A_{q(-1)n}-B_{q1n}+B_{q(-1)n}\right]e^{jk_0 z_{q0}}\right\}
\end{aligned}
\tag{26}
$$

e. Specific rain attenuation

Suppose that Q spheres are randomly allocated inside the volume V (m^3). By using σ^e (m^2) in Eq. (26), the specific rain attenuation is given by $\gamma = \sigma^e / V$ (m^{-1}). From a practical viewpoint, the unit is often converted via

$$
\gamma\,[\mathrm{dB/km}] = \gamma\,[\mathrm{m}^{-1}]\times 10^3 \times 10\log_{10} e = 4343\,\sigma^e / V \tag{27}
$$

If we can neglect the multiple scattering among spheres, the approximate cross section

$$
\sigma^e \approx -\frac{2\pi}{k_0^2}\mathrm{Re}\sum_{n=1}^{\infty}(2n+1) = \sum_{q=1}^{Q}\left(\overline{A}_{qn}+\overline{B}_{qn}\right) \tag{28}
$$

is applied to Eq. (27) with the aid of Eqs. (16) and (17). We will use this formula in the later computations.

Let us determine the series of realistic radii a_q as a function of rainfall intensity R (mm/h). Each distribution model proposes a function $N(a)$ (m^{-3} mm^{-1}), which is a number of raindrops having the radius between a and $a + da$ (mm) per unit volume. Then the integral

$$
\widetilde{N}(a) = \int_0^a N(a')\,da' \quad [\mathrm{m}^{-3}] \tag{29}
$$

gives a number of raindrops, the radius of which are less than a (mm), per unit volume. The value $\widetilde{N}(\infty)$ denotes the total number. When we deal with Q raindrops in the numerical computation, the q-th radius a_q (mm) is sampled by the rule

$$\frac{\tilde{N}(a_q)}{\tilde{N}(\infty)} = \frac{q-1/2}{Q} \quad (q = 1, 2, ..., Q) \tag{30}$$

with $V = Q / \tilde{N}(\infty)$. Among a lot of proposed models, we select exponential and Weibull distribution models and the related formulas are arranged in Table 4.

Raindrop distribution model	Density function $N(a)$ ($\mathrm{m^{-3}\,mm^{-1}}$) Parameters	Sampled radius a_q (mm) by (30)
Exponential (Marshall et al., 1948)	$N_0 e^{-\Lambda a}$ $N_0 = 16000\ \mathrm{m^{-3}\,mm^{-1}}$ $\Lambda = 8.2\ R^{-0.21}$ $\tilde{N}(\infty) = N_0 / \Lambda$	$-\frac{1}{\Lambda}\log\left(1-\frac{q-1/2}{Q}\right)$
Weibull (Sekine et al., 1987)	$N_0 \frac{\eta}{\sigma}\left(\frac{a}{\sigma}\right)^{\eta-1} e^{-(a/\sigma)^{\eta}}$ $N_0 = 1000\ \mathrm{m^{-3}\,mm^{-1}}$ $\eta = 0.95\ R^{0.14}$ $\sigma = 0.13\ R^{0.44}$ $\tilde{N}(\infty) = N_0$	$\sigma\left[-\log\left(1-\frac{q-1/2}{Q}\right)\right]^{1/\eta}$

Table 4. Representative two distribution models. The rainfall R is measured in mm/h.

f. Numerical examples

Examples of the radius a_q by the above models are given in Table 5 for fixed R and Q. The exponential distribution proposed by Marshall and Palmer predicts that, compared with Weibull model, smaller raindrops are concentrated inside a smaller volume.

Fig. 6 shows the convergence of attenuation γ as Q increases based on the Weibull distribution up to 1000 GHz. The relative complex permittivity of water is a function of temperature and frequency. One of the effective formulas (Liebe et al., 1991) gives, at $25^{\circ}\mathrm{C}$, ε_r = 78.1–*j*3.8, 62.8–*j*29.9, 7.8–*j*13.8, and 4.2–*j*2.3 for 1, 10, 100, and 1000 GHz, respectively. Slight irregularity at Q = 2 stems from internal resonance in the dielectric media, which is relaxed for larger Q due to the averaging effect. Roughly speaking, the distance between adjacent curves becomes halved as Q is doubled, which results in good convergence. Hereafter we will fix as Q = 32.

Model	Radii a_q (mm)	V ($\mathrm{cm^3}$)
Exponential	0.02 0.06 0.10 0.16 0.23 0.32 0.46 0.77	1800
Weibull	0.14 0.28 0.40 0.52 0.65 0.80 0.99 1.35	8000

Table 5. Radii of raindrops at R = 50 mm/h and Q = 8.

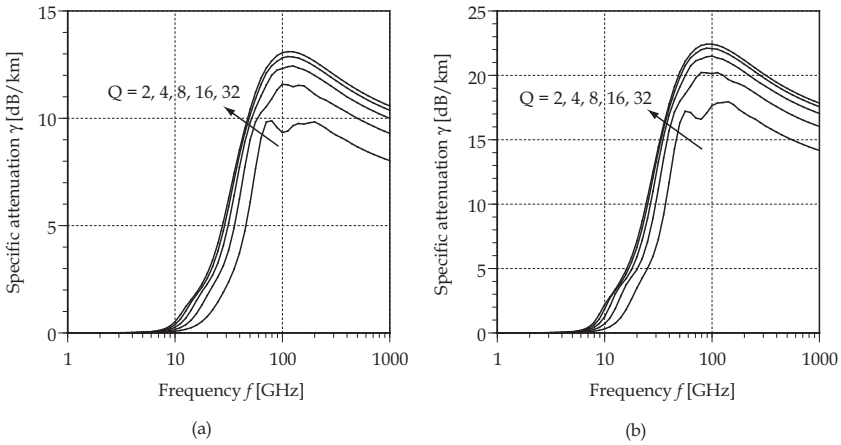

Fig. 6. Convergence of specific attenuation at 25°C by Weibull distribution as the number of sampled raindrops Q is increased. (a) R =25 mm/h and (b) R = 50 mm/h.

Fig. 7 shows comparisons of attenuation γ between the exponential and Weibull distribution for four values of rainfall R. At low frequencies the exponential distribution predicts lower attenuation, probably because electrically small raindrops work as weak scatterers and absorbers. These drops contribute, in turn, to attenuation at high frequencies, since they are now electrically large and densely allocated. Fig. 8 shows the effect of changing temperature. The deviation of specific attenuation behaves in a different manner between the frequency bands 10-20 GHz and 30-100 GHz. This is explained by the permittivity of the water. In the lower frequency band around 15 GHz, the real part of ε_r is large at high temperatures, which leads large scattering loss. On the other hand, in the millimeter wave around 50 GHz, the increase in the permittivity makes the raindrops electrically large, which promotes the electromagnetic transparency of rain medium and results in low attenuation.

2.4 Synthetic storm technique

Synthetic storm technique (SST) is a method to obtain estimates of rain attenuation statistics for links of a given length, whenever a real radio link is inexistent. Given measurements of wind velocity and time series of rain intensity at a site, statistics of rain attenuation on a hypothetical link passing through or nearby that site can be estimated by dividing the link into segments, each of length equal the distance travelled over by the rain structure as it is blown by the wind during one sampling period of rain rate measurement. At each sampling time, rain attenuation is obtained as the sum of specific attenuation estimates (dB/km) multiplied by the segment length (km). That is, the n-th sample of rain attenuation is:

$$A(n) = \sum_{m=0}^{N-1} k\left[R(n-m)\right]^{\alpha} \delta_m \tag{31}$$

with $R(n)$ denoting the n-th sample of rain rate measurement, k and a the power-law coefficients that depend on radio frequency, wave polarization, temperature, drop shape

and size distribution, such as those given by ITU-R Rec. P.838 (ITU-R, 2005), N the number of segments constituting the link, and δ_m the length of the m-th segment of the link. That is,

$$N = \left\lceil \frac{L\cos\theta}{vT} \right\rceil \tag{32}$$

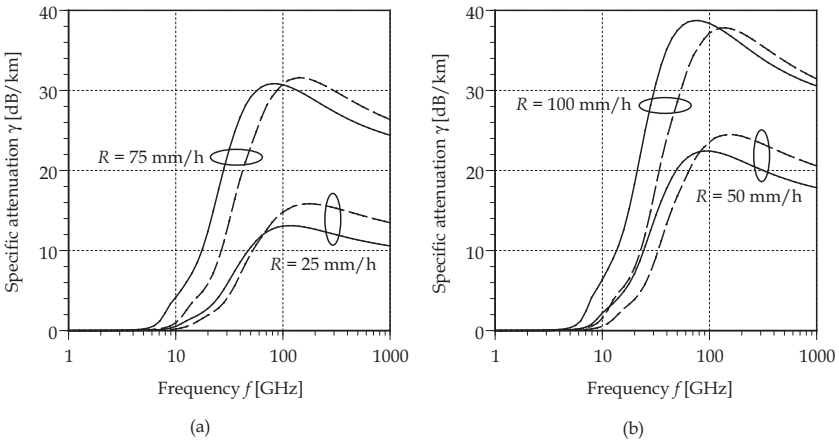

Fig. 7. Specific attenuation at 25°C by two models with sampled 32 raindrops. Dashed curves: exponential distribution, Solid curves: Weibull distribution.

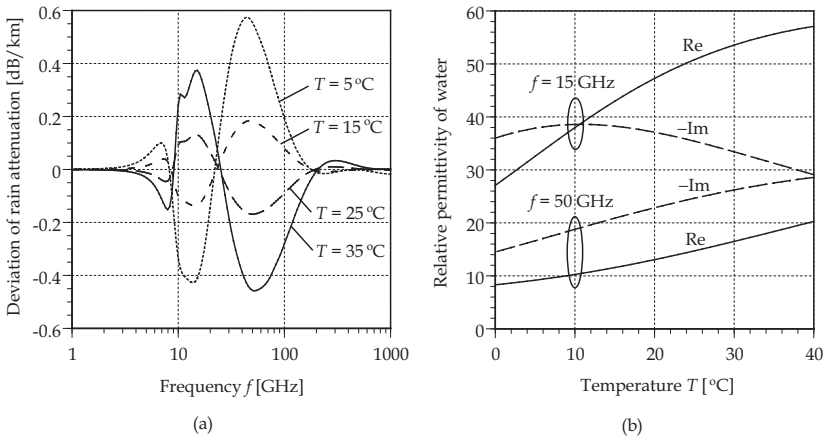

Fig. 8. Temperature dependence of specific attenuation by Weibull distribution with sampled 32 raindrops at R = 50 mm/h. (a) Deviation $\gamma(T) - \gamma(20^{\circ}\mathrm{C})$ and (b) Real and Imaginary parts of relative permittivity ε_r.

$$\delta_m = \begin{cases} \dfrac{vT}{\cos\theta} & m = 0,\ldots,N-2 \text{ and } \theta \neq 90° \\ L - \dfrac{(N-1)vT}{\cos\theta} & m = N-1 \text{ and } \theta \neq 90° \\ L & \text{all } m \text{ and } \theta = 90° \end{cases} \tag{33}$$

with v representing wind velocity, T the rain rate sampling period and θ angular difference between the wind direction and link orientation. The situation is graphically described in Fig. 9. The SST does not yield estimates of the actual rain attenuation, but it proves to give a good estimate of the attenuation statistics (Matricciani & Riva, 2005). It can also be used to acquire good statistical estimates of fade dynamics (Matricciani, 2004; Sánchez-Lago et al, 2007). Mahmudah et al (2008) and Suwadi et al (2009) use SST to examine the performance of cell-site diversity in a network of converging, short links.

Eqn. (31) indicates that rain attenuation samples can be straightforwardly obtained by convolving the rectangular-windowed time series of the specific attenuation and that of the segment length. This fact has been pointed out first by Matricciani (1996) and is also confirmed in our own study. When the wind direction and link orientation are perpendicular, the link comprises only a single segment and the convolution becomes multiplication. In this case, the resulting attenuation statistics tend to be higher due to the absence of moving-average effects.

Before proceeding to use the SST results in subsequent analyses, a comparison is made on the different results arising from the use of different values of wind velocity. In this case, we consider three different statistics, namely, the daily average, the daily maximum, and the monthly average. It is shown in Fig. 10 that the distributions of attenuation for the case of daily average and monthly average wind velocity, respectively, are almost identical, whereas the one obtained using daily maximum value tend to give an upper bound (Hendrantoro et al, 2007b). It can also be observed that for probabilities of being exceeded less than 0.1%, the SST results are higher than the value predicted by the ITU-R method.

An attempt to confirm the applicability of SST for short links is made by comparing the attenuation statistics on a hypothetical link from the SST exercise using rain rate measurements with that estimated using a simple segmentation method. The latter makes use of the fact that the measurement sites are almost aligned in an almost North-South orientation (see Fig. 1). Using this method and recognizing that the fictitious link A-D would be 1.55 km long, the rain attenuation estimate at the n^{th} sampling time is:

$$A(n) = 1.55k \sum_{m=1}^{3} \left[R_m(n)\right]^{\alpha} \Delta l_m \quad \text{dB} \tag{34}$$

with indexes m = 1, ..., 3 referring to sites A, B and D (rain gauge at site C is inactive during the observation), $\Delta l_1 = \Delta l_3 = 0.25$, $\Delta l_2 = 0.5$, and all other variables defined previously. This scenario is depicted in Fig. 11. It is assumed that each rain gauge represents an area of homogeneous instantaneous rain rate. Results shown in Table 6 indicate that there is no significant difference among the percentiles for various methods, sources, and link orientations. This has also been confirmed through a Kolmogorov-Smirnov test in which the